A yeast-based system to study SARS-CoV-2 Mpro structure and to identify nirmatrelvir resistant mutations

Jin Ou

The Catholic University of America

Eric Lewandowski

University of South Florida

Yanmei Hu

Rutgers University

Austin Lipinski

University of Arizona

Ryan Morgan

University of South Florida   https://orcid.org/0000-0002-5662-5443

Lian Jacobs

University of South Florida

Xiujun Zhang

University of South Florida

Melissa Bikowitz

University of South Florida   https://orcid.org/0000-0003-4985-3461

Paul Langlais

University of Arizona

Haozhou Tan

Rutgers University

Jun Wang

Rutgers, the State University of New Jersey   https://orcid.org/0000-0002-4845-4621

Yu Chen

University of South Florida   https://orcid.org/0000-0002-5115-3600

John Choy (✉ choy@cua.edu)

Catholic University of America

Article

Keywords:

1   **A yeast-based system to study SARS-CoV-2 Mpro structure and to identify nirmatrelvir**

2   **resistant mutations**

3   Jin Ou[1], Eric M. Lewandowski[2], Yanmei Hu[3], Austin A. Lipinski[4], Ryan T. Morgan[2], Lian M.C.

4   Jacobs[2,5], Xiujun Zhang[2], Melissa J. Bikowitz[2], Paul Langlais[4], Haozhou Tan[3], Jun Wang[3*], Yu

5   Chen[2*], John S. Choy[1*]

6

7   [1]Department of Biology, School of Arts and Sciences, The Catholic University of America,

8   Washington, DC 20064, United States

9   [2]Department of Molecular Medicine, Morsani College of Medicine, University of South Florida,

10   Tampa, FL, 33612, United States

11   [3]Department of Medicinal Chemistry, Ernest Mario School of Pharmacy, Rutgers, the State

12   University of New Jersey, Piscataway, NJ, 08854, United States

13   [4]Department of Medicine, College of Medicine, University of Arizona, Tucson, AZ 85724,

14   United States

15   [5]Drug Discovery Department, Moffit Cancer Center, Tampa, FL 33612, United States

16

17   [*]Corresponding Authors:

18   John S. Choy, email: choy@cua.edu, Tel: 202-319-5278

19   Yu Chen, email: ychen1@usf.edu, Tel: 813-974-7809

20   Jun Wang, email: junwang@pharmacy.rutgers.edu, Tel: 828-445-6488

21

22

Abstract

The SARS-CoV-2 main protease (M^{pro}) is a major therapeutic target. The M^{pro} inhibitor, nirmatrelvir, is the antiviral component of Paxlovid, an orally available treatment for COVID-19. As M^{pro} inhibitor use increases, drug resistant mutations will likely emerge. We have established a non-pathogenic system, in which yeast growth serves as a proxy for M^{pro} activity, enabling rapid identification of mutants with altered enzymatic activity and drug sensitivity. The E166 residue is known to be a potential hot spot for drug resistance and yeast assays showed that an E166R substitution conferred strong nirmatrelvir resistance while an E166N mutation compromised activity. On the other hand, N142A and P132H mutations caused little to no change in drug response and activity. Standard enzymatic assays confirmed the yeast results. In turn, we solved the structures of M^{pro} E166R, and M^{pro} E166N, providing insights into how arginine may drive drug resistance while asparagine leads to reduced activity. The work presented here will help characterize novel resistant variants of M^{pro} that may arise as M^{pro} antivirals become more widely used.

Introduction

The evolution of new SARS-CoV-2 variants that evade vaccines, cause breakthrough COVID-19 infections in vaccinated individuals, and the limited vaccine availability in many parts of the world, highlight the need for complementary approaches[1]. Antiviral drugs provide an important alternative and can contribute to minimizing disease severity and death. The SARS-CoV-2 main or 3C-like protease (M^{pro} or $3CL^{pro}$) is essential for viral replication and is a promising drug target [2,3]. There have been intense efforts to repurpose or to develop new drugs that directly target M^{pro} [4,5]. In December 2021, emergency authorization use of Paxlovid to treat COVID-19 was granted by the US Food and Drug Administration [6]. Paxlovid is a combination of the M^{pro} inhibitor, nirmatrelvir, and the cytochrome CYP3A inhibitor, ritonavir, which slows metabolism of nirmatrelvir [7,8]. Currently, there are several other M^{pro} inhibitors in clinical trials, including PF-07304814, the phosphate form of PF-00835231[9,10]. As M^{pro} inhibitors become more widely used the emergence of resistant mutations will increase as greater selection pressure is present in the population.

Knowledge of resistant mutants can inform on drug design modifications to identify new drugs that target resistant variants. However, standard approaches to characterize resistant mutants using live virus[11], recombinant proteins, and in vitro assays can be highly limiting due to infrastructure requirements, cost, and time[12]. Here we report a yeast system that is non-pathogenic, rapid, inexpensive, and reports on M^{pro} activity and drug resistance simply by measuring yeast growth. Using this assay, we found that compared to wild-type, the E166R mutation conferred strong nirmatrelvir resistance (K_i > 1000-fold). As the E166 site appears to be a hot spot for drug resistance from *in vitro* viral evolution experiments[13,14], we solved the structures of two substitution mutants M^{pro} E166N and M^{pro} E166R, revealing how E166

60   mutations may compromise activity versus drug resistance, respectively. Our results demonstrate

61   the yeast system can be a reliable tool to determine the activity and drug responses of M^{pro}

62   mutants. Results from the yeast assays can help rapidly prioritize mutants for further analysis

63   using more resource intensive systems. In doing, so we can efficiently test M^{pro} mutants as they

64   arise in the population and aid in mitigating COVID-19 infections.

65

66   **Results**

67   **SARS-CoV-2 M^{pro}, PL^{pro}, spike, and helicase proteins are toxic in *S. cerevisiae***

68   We expressed six SARS-CoV-2 (Wuhan-Hu-1) NSPs and the structural genes, spike, M,

69   E and N[15] to determine if any would result in growth effects (Fig. 1A and Fig. S1A). We

70   observed no marked growth phenotypes as determined by spot tests when M, E, N, NSP7, NSP8,

71   or NSP12 were expressed (Fig. S1B). In contrast, spot tests revealed nearly a complete absence

72   of growth when cells expressed NSP3 (PL^{pro}), NSP5 (M^{pro} or $3CL^{pro}$), NSP13 (Helicase), and

73   spike (Fig. S1B). Analysis of growth profiles of cells expressing PL^{pro}, M^{pro}, Helicase, and spike

74   showed all four genes caused a reduction in growth. M^{pro} and the Helicase were the most toxic

75   conferring a ~70 to 80% reduction in total growth by 72 hours compared to cells carrying empty

76   vector (Fig. 1A, 1B). As M^{pro} is highly conserved between classes of coronavirus and a key drug

77   target we focused our efforts on using the yeast system to study M^{pro} structure and function.

78

79   **Growth defect conferred by M^{pro} expression depends on its catalytic activity and associated**

80   **with decreased abundance in essential and non-essential yeast proteins**

81   To determine if the growth reduction depended on M^{pro} proteolytic activity we

82   constructed a catalytic mutant of M^{pro} by replacing the key cysteine at position 145 to an alanine,
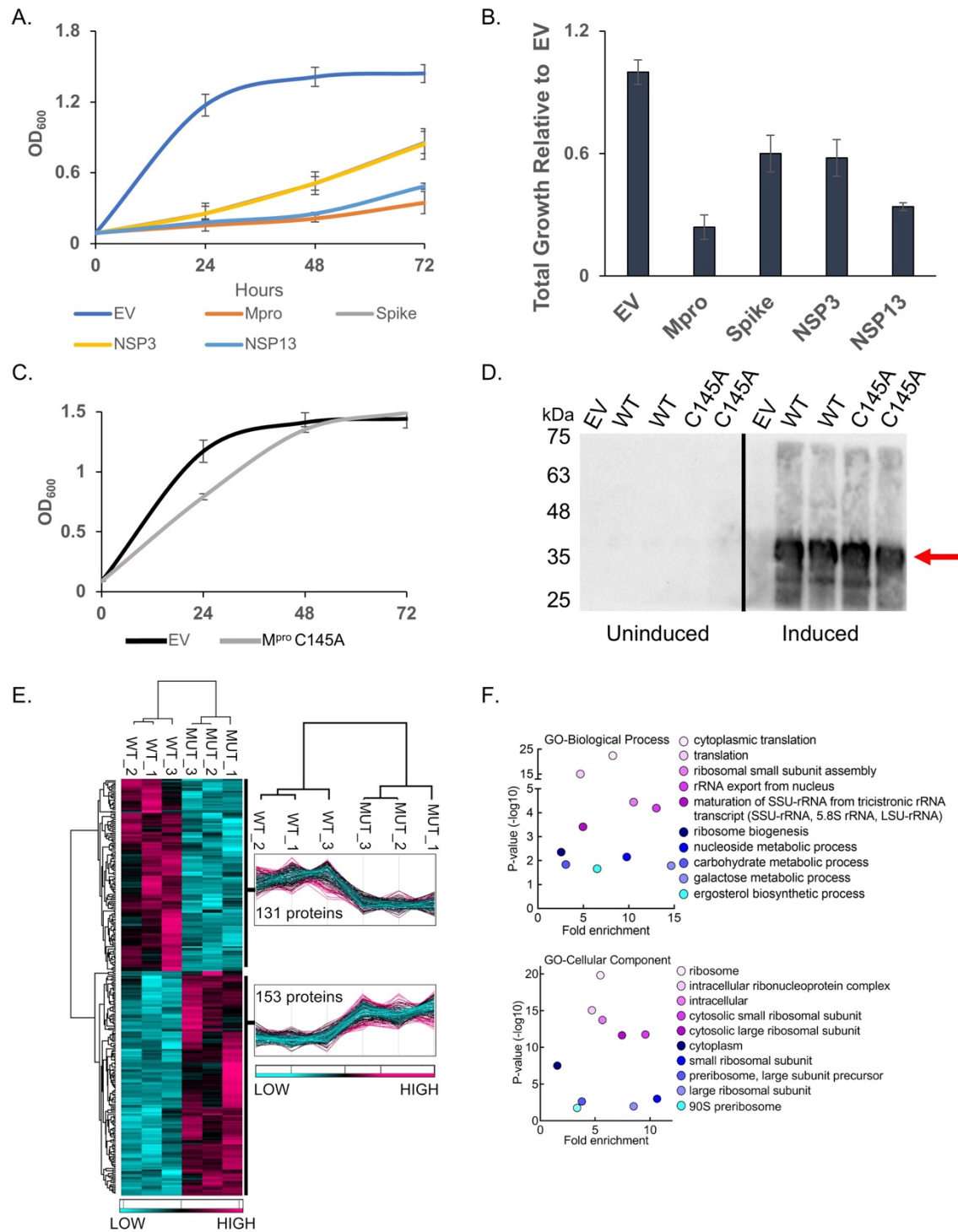
Fig. 1. M^pro confers a significant reduction in growth in yeast caused by decreases in a variety of cellular proteins. A) The indicated SARS-CoV-2 genes under a galactose inducible promoter were expressed in yeast and conferred growth defects compared to empty vector (EV). B) Bar graph shows the total growth of cultures after 72 hours normalized to EV. C) Expression of the catalytically inactive M^pro C145A mutant does not confer a growth reduction and yeast

5

88   grow similarly to EV control cells. D) Protein levels of the M^{pro} C145A mutant and wild-type
89   M^{pro} (WT) are comparable. Shown are two biological replicates for each form of M^{pro}. E) Total
90   protein lysates made from yeast expressing the wild-type M^{pro} (WT) or M^{pro} C145A mutant
91   (MUT) were subjected to mass spectrometric analyses revealing 153 proteins were higher in
92   abundance in the mutant relative to the wild-type. F) Gene Ontology (GO) analyses indicates an
93   enrichment of proteins with functions in translation that are significantly reduced in the presence
94   of M^{pro} versus M^{pro} C145A. Plots in A and B show averages from three biological replicates and
95   error bars are standard deviations.

96

97   which prevents the initial protonation step needed for peptide bond hydrolysis[16,17]. Liquid growth

98   assays showed that yeast expressing the M^{pro} C145A mutant grew as well as the yeast control

99   carrying empty vector (Fig. 1C). Western analysis showed that yeast expressed similar levels of

100 wild-type and M^{pro} C145A mutant (Fig. 1D). These results demonstrate that the growth reduction

101 observed in yeast expressing M^{pro} is dependent on its proteolytic activity.

102   Next, we measured the relative abundance of proteins in yeast expressing M^{pro} compared

103 to yeast expressing the M^{pro} C145A catalytic mutant to determine the mechanism(s) that lead to

104 loss of cell viability. Whole cell lysates were made from three independent cultures of cells

105 expressing wild-type M^{pro} or the catalytic M^{pro} C145A mutant (Fig. 1E and Fig. S2). The

106 biological replicates were highly reproducible, and we observed peptides from 153 proteins

107 (Table S1) were significantly reduced in yeast expressing M^{pro} compared to the M^{pro} C145A

108 mutant (Fig. 1E.) Gene ontology analysis revealed an enrichment for genes with functions in

109 translation (Fig. 1F). In particular, multiple ribosomal proteins and translational regulators were

110 reduced. There were a number of proteins that were significantly enriched in the M^{pro} catalytic

111 mutant with functions in a variety of activities beyond translation (Table S1) and several are

112 known to be essential (Table S1). These results show that expression of M^{pro} leads to decreases

113 in a variety of proteins and eventual loss of translation that is likely the cause of the growth

114 defects.

Nirmatrelvir restores growth to yeast expressing M^pro from multiple coronaviruses

Considering that the growth reduction conferred by M^{pro} activity is dependent on its proteolytic activity we tested if treating yeast with nirmatrelvir, would suppress the growth reduction. We tested nirmatrelvir at several concentrations and observed no cytotoxic effects (Fig. S3A). Treating cells with increasing doses of nirmatrelvir led to a corresponding increase in growth (Fig. 2A). At 100μM and 200μM of nirmatrelvir, growth was restored to similar levels as cells carrying empty vector (Fig. 2A). As a metric to compare the effects of nirmatrelvir, we estimated the concentration of drug required to restore 50% of growth (RC_{50}) relative to that of untreated M^{pro} expressing cells. Based on this criterion we calculated RC_{50} for nirmatrelvir to be 110.47 ± 4.76μM (Fig. 2A and 2H). To determine if M^{pro} from other coronaviruses could be studied similarly, we tested the recent Omicron variant, M^{pro} P132H, which is currently the dominant form of M^{pro}, and M^{pro} from SARS-CoV-1 and Bat-CoV-HKU9. We observed that in all cases M^{pro} conferred a significant growth reduction (Fig. 2C and Fig. S3B). Nirmatrelvir has been reported to have broad M^{pro} specificity[7,9]. Consistent with this work, we observed that nirmatrelvir could restore growth in yeast expressing M^{pro} from all three forms of M^{pro} (Fig. 2E, 2H, and Fig. S3B).

To determine the specificity of the restored growth conferred by nirmatrelvir in cells expressing M^{pro}, we tested the effects of nirmatrelvir on cells expressing PL^{pro}. The growth reduction associated with expression of the PL^{pro} (Fig. 1A) should not be inhibited by this drug. We treated cells expressing PL^{pro} with 200μM of nirmatrelvir and observed no improvement in growth (Fig. 2B). On the other hand, 50 μM and 100μM of GRL0617, an inhibitor of PL^{pro} [18] was associated with partial recovery of growth (Fig. 2B). Together, these observations show that

7

137　　the restoration of growth conferred by nirmatrelvir in cells expressing M^{pro} is specific to M^{pro}

138　　rather than a non-specific effect on yeast physiology.

139

140　　**Characterization of potential nirmatrelvir resistant mutations in M^{pro}**

141　　　　We tested if growth of yeast expressing M^{pro} could be used as a proxy for M^{pro} activity.

142　　Thus, providing a system to rapidly determine structure function relationships as they relate to

143　　activity and drug resistance. A variety of interactions (H-bonds, salt-bridges, van der waals)

144　　mediate binding between the catalytic site of M^{pro} and inhibitors [19-21]. While knowledge of the

145　　residues in contact with the inhibitor can inform predictions that may compromise inhibitor

146　　binding it is not obvious what amino acid substitutions would maintain M^{pro} activity toward

147　　substrate while compromising inhibitor interactions. With our yeast system we can easily test the

148　　effect of substitution mutations and rapidly determine if the mutations alter catalytic activity and

149　　sensitivity to inhibitor(s) by following growth phenotypes. To determine the feasibility of this

150　　approach we focused on E166, and N142 as these two residues form direct interactions with

151　　inhibitors and substrates [19,22].

152　　　　We tested substitutions of E166 with three different amino acids that are yet to be

153　　dominant or present in the population. The following mutants predicted to be conserved

154　　(E166D), as the negative charge is maintained but with one less carbon in the side-chain; non-

155　　conserved (E166N), as asparagine is uncharged and has one less side chain carbon; and another

156　　non-conserved (E166R) substitution in which the arginine side chain is longer and positively

157　　charged were tested. We observed that all three substitutions were expressed at the same levels

158　　as wild-type M^{pro} but M^{pro} E166D and M^{pro} E166N mutants did not cause a reduction in growth

159　　and grew as well as empty vector controls (Fig. 2C, 2D, Fig. S4A). These results indicate that
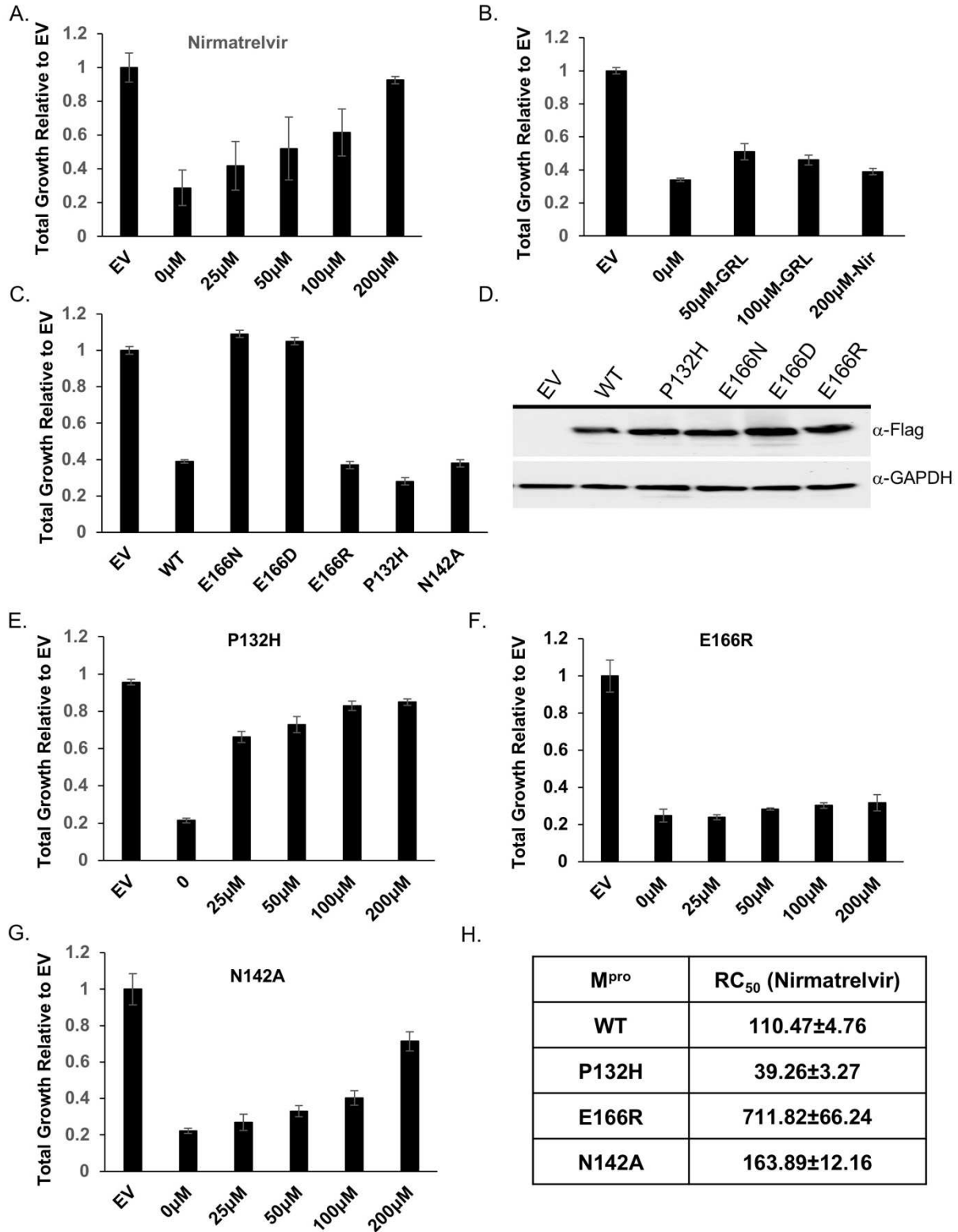
Fig. 2. Yeast growth assays identify nirmatrelvir resistant M^pro mutants. A) Total growth of
cultures after 72 hours expressing M^pro in the presence of increasing doses of nirmatrelvir
normalized to growth of yeast carrying empty vector (EV) are plotted. Nirmatrelvir is effective at

9

163 protecting yeast from the toxicity of M^{pro} as growth is restored to levels comparable to EV. B)
164 Yeast expressing PL^{pro} show a growth reduction and treatment with nirmatrelvir (nir) does not
165 rescue the growth defect. On the other hand, treating cells with GRL0617 (GRL) restores some
166 growth. C) Yeast expressing substitutions E166D and E166N grow as well as EV but E166R,
167 P132H, and N142A results in significant growth reduction comparable to wild-type M^{pro}. D)
168 Western analysis shows that mutants and wild-type M^{pro} are expressed at comparable levels. E -
169 G) Cells expressing P132H and N142A remain sensitive to nirmatrelvir, indicated by growth
170 recovery, but E166R appears to be resistant as there is a lack of growth even when treated with
171 200µM of nirmatrelvir. H) RC_{50} measurements of each mutant in response to nirmatrelvir
172 treatment. For all experiments, at least three biological and three technical replicates were
173 performed for EV, wild-type and mutant M^{pro}. Error bars represent standard deviations.
174

175 M^{pro} E166D and M^{pro} E166N may have defects in their enzymatic activities. However, the M^{pro}

176 E166R mutant conferred a growth reduction that matched the wild-type M^{pro}, suggesting that its

177 catalytic activity was intact (Fig. 2C and Fig. S4B).

178   Next, we challenged cells expressing M^{pro} E166R with increasing concentrations of

179 nirmatrelvir (25µM, 50µM, 100µM, or 200µM) and observed no significant improvement in

180 growth remaining nearly identical to the untreated culture of M^{pro} E166R expressing cells (Fig.

181 2F and Fig. S4B). Based on these experiments, the RC_{50} for nirmatrelvir is 711.82 ± 66.24µM, a

182 ~7-fold increase in RC_{50} compared to wild-type M^{pro} (Fig. 2H). These results suggest that the

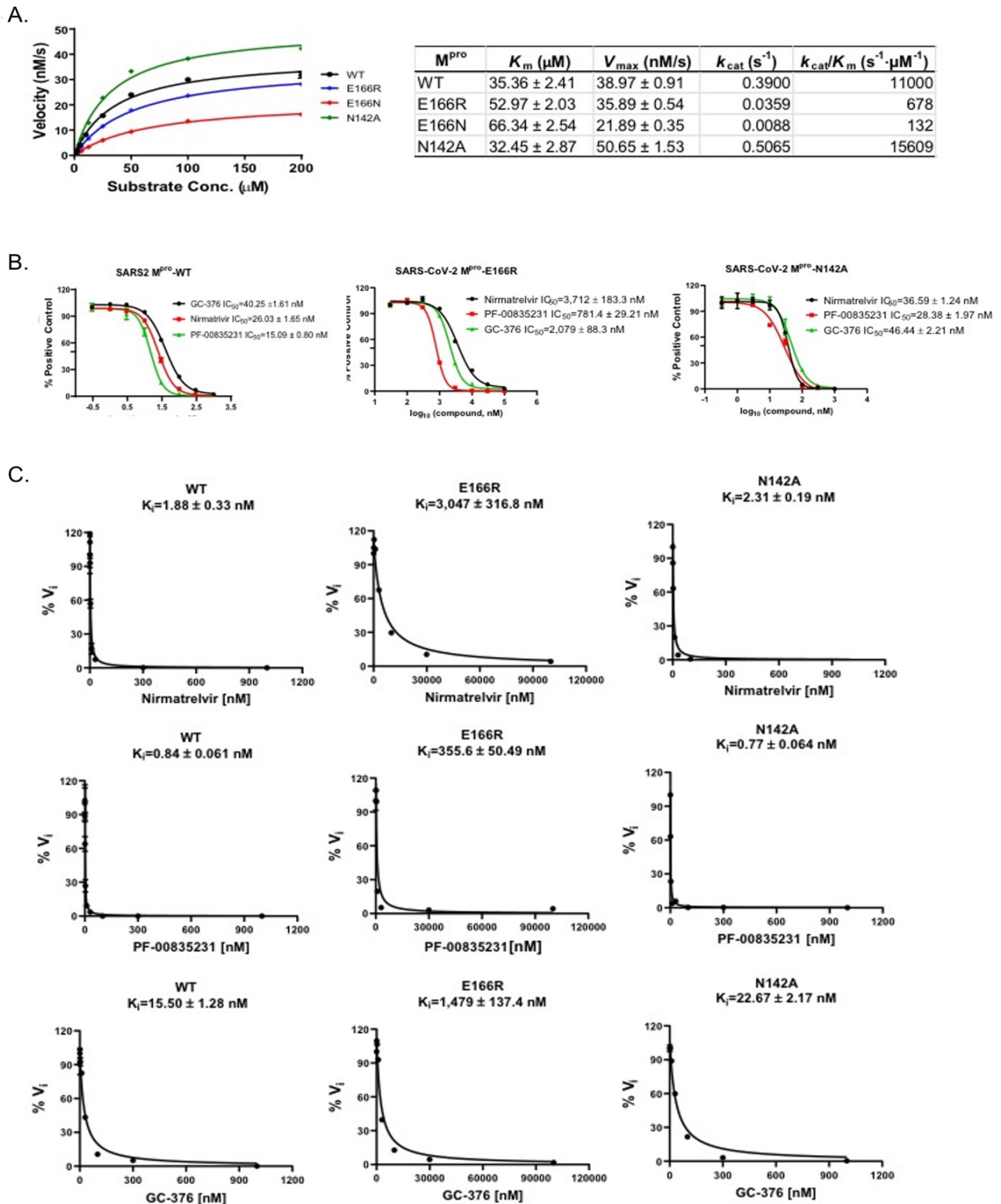183 E166R mutation confers resistance to nirmatrelvir.

184   We constructed a substitution at position N142, which is known to contribute to inhibitor

185 and substrate binding[7] and is yet to be present in the population. To inform on the specific

186 substitution to make we used a distantly related M^{pro} from the gamma-coronavirus, IBV, which is

187 conserved but displays slight divergence from SARS-CoV-2 M^{pro}[9]. We replaced N142 with

188 alanine (M^{pro} N142A), as alanine is found in the IBV M^{pro} at the homologous site[23]. We observed

189 M^{pro} N142A was expressed at levels comparable to wild-type and conferred a similar reduction

190 in growth (Fig. 2C and Fig. S4C, S4E) showing that it remained active. The RC_{50} for nirmatrelvir

191 increased modestly by ~1.5-fold (Fig. 2G, 2H). These results show that the substitution mutant

192   E166R leads to nirmatrelvir resistance while N142A results in little difference from wild-type

193   and E166N and E166D cause a loss in activity.

194

In vitro protease assays confirm that M^{pro} E166R is highly resistant to nirmatrelvir

196   The results from the yeast assays suggest Mpro E166R confers resistance to nirmatrelvir

197   (~7-fold increase in RC50 vs WT). To determine how well yeast growth assays correlated with

198   standard enzymatic assays we directly measured protease activity using recombinant Mpro,

199   Mpro E166N, Mpro E166R, and Mpro N142A. First, we measured the catalytic efficiencies for

200   all four forms of Mpro (Fig. 3A). Compared to wild-type Mpro , the catalytic efficiencies

201   (k_{cat}/K_m) of Mpro E166R was decreased by ~16-fold, while Mpro N142A displayed a slight

202   increase of 1.4-fold. In contrast, E166N was nearly inactive with k_{cat}/K_m of 132 S^{-1}M^{-1}, a 83.5-

203   fold reduction compared to WT. The enzymatic assay results confirmed that the lack of toxicity

204   of E166N in the yeast growth assay was due to the loss of catalytic activity (Fig. 2C). To

205   determine the response of the mutants (M^{pro} E166R, and M^{pro} N142A) to inhibitors compared to

206   wild-type, we measured the IC$_{50}$ and K_i for nirmatrelvir, and two other M^{pro} inhibitors PF-

207   00835231, and GC-376[9,24]. We observed for M^{pro} E166R, increases in IC$_{50}$'s of ~143-fold for

208   nirmatrelvir, ~52-fold for PF-0083521, and ~52-fold for GC-376. On the other hand, M^{pro}

209   N142A, only minor increases in IC$_{50}$'s of ~1.4-fold for nirmatrelvir, ~1.9-fold for PF-0083521,

210   ~1.1-fold for GC-376 (Fig. 3B). The K_i values for the inhibitors in assays with M^{pro} E166R were

211   increased by ~1620-fold for nirmatrelvir, ~423-fold for PF-0085231, and ~37-fold for GC-376

212   (Fig. 3C). Nearly no difference in K_i values from assays with M^{pro} N142A, ~1.2-fold for

213   nirmatrelvir, ~0.9-fold for PF-0085231, ~1.5-fold for GC-376) (Fig. 3C). The enzymatic assays

214   confirm the results from the yeast assays showing that M^{pro} E166R is highly resistant to

A.

M^{pro}	K_m (μM)	V_{max} (nM/s)	k_{cat} (s^{-1})	k_{cat}/K_m (s^{-1}·μM^{-1})
WT	35.36 ± 2.41	38.97 ± 0.91	0.3900	11000
E166R	52.97 ± 2.03	35.89 ± 0.54	0.0359	678
E166N	66.34 ± 2.54	21.89 ± 0.35	0.0088	132
N142A	32.45 ± 2.87	50.65 ± 1.53	0.5065	15609

B.

C.

Fig. 3. Enzymatic assays demonstrate that M^{pro} E166R is highly resistant to PF-00835231, nirmatrelvir, and GC-376. A) Michaelis–Menten plot of M^{pro} and its mutants with various concentrations of FRET substrate. The K_m, V_{max}, k_{cat}, and k_{cat}/K_m values are shown in the table

12

218 on the right. B) The IC_{50} plots of nirmatrelvir, GC-376, and PF-00835231 against M^{pro}, M^{pro}
219 E166R, and M^{pro} N142A. C) K_i plots of nirmatrelvir, GC-376, and PF-00835231 against M^{pro},
220 M^{pro} E166R, and M^{pro} N142A.
221

222 nirmatrelvir and also show that there is cross-resistance to PF-0085231 and GC-376 (Fig. 3B,

223 3C). Similarly, results from yeast assays of M^{pro} N142A mutant appears to correspond well to the

224 *in vitro* assays as both show minor to no increases in resistance (Fig. 3B, 3C). Furthermore, the

225 M^{pro} E166N, which is not predicted to be catalytically active from the yeast assay, displayed >83-

226 fold decrease in activity compared to wild-type in the *in vitro* assays. This result is completely

227 consistent with observing no growth reduction when expressed in yeast. Taken together there is

228 good correlation between the enzyme and yeast assays.

229

230 **Crystal Structure of Mpro^{E166R} reveals a loss of interactions leading to drug resistance**

231   We were particularly interested in how replacing glutamate at position 166 with arginine

232 led to a >1000-fold increase in resistance to nirmatrelvir while a substitution with asparagine led

233 to an 83.5-fold decrease in enzymatic activity even though E166 is not known to be directly

234 involved in catalysis. Toward addressing both questions, we solved the crystal structure of apo

235 M^{pro} E166N and the complex structure of M^{pro} E166R with GC-376 at 2.3 and 2.1 Å resolution,

236 respectively (Fig. 4). In the M^{pro} E166N mutant structure, N166 forms a hydrogen bond (HB)

237 with H163, an interaction not observed between E166 and H163 in the wild-type M^{pro} structure

238 (Fig. 4A). This new HB prevents H163 from hydrogen bonding with the glutamine side chain of

239 the substrate, an interaction crucial to substrate binding. The binding of the substrate would

240 therefore require N166 to adopt a different conformation, breaking the HB with H163 and

241 increasing the energetic cost. These observations explain the drastic decrease of activity in the

242   E166N mutant and lack of toxicity when expressed in yeast (Fig. 2C) bringing to light how

243   residues outside of the catalytic core can influence substrate binding.

244   In contrast, the longer and positively charged R166 side chain in the M^pro E166R mutant

245   does not interact with H163, but rather extends into the solvent (Fig. 4B). Therefore, the S1 site

246   is open for substrate binding. However, the E166R mutation does affect ligand binding in several

247   aspects. The negatively charged E166 side chain forms two crucial HBs, one with the N-terminus

248   of the neighboring M^pro protomer in the biological dimer, and the other with the pyrrolidone side

249   chain of inhibitors (in both nirmatrelvir and GC-376) or with the glutamine side chain of the
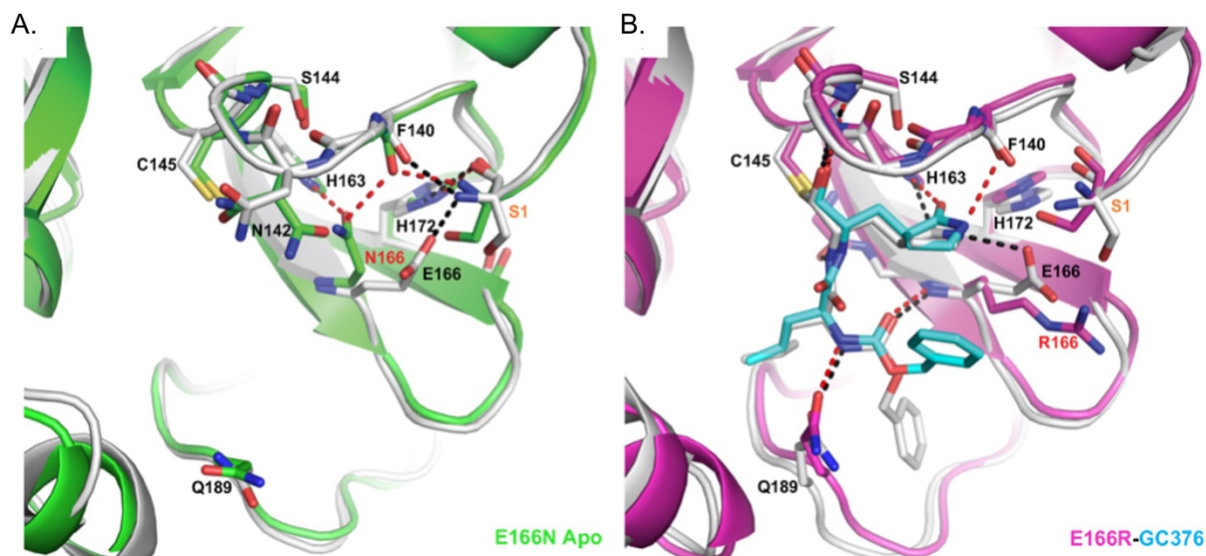
250
251   **Fig. 4. Crystal structures of E166R reveals structural basis for resistance and of E166N**
252   **reveals basis for inactivity.** A) Apo Mpro WT (white, PDB 7JP1) aligned with apo Mpro
253   E166N (green, PDB 8DDI). B) Mpro WT GC376 complex (white, PDB 6WTT) aligned with
254   Mpro E166R GC376 complex (magenta, PDB 8DDM). WT hydrogen bonds are shown as black
255   dashes, and mutant hydrogen bonds are shown as red dashes. GC376 is shown in white for the
256   WT structure and cyan for the mutant structure. Mutations are indicated with red text. Ser1 from
257   an adjacent protomer is indicated with orange text.

258

259   substrate as described above. The E166R mutation would abolish this direct HB with the

260   substrate or inhibitor, resulting in the pyrrolidone ring of GC-376 forming an alternative weak

261   HB with F140 (3.1 Å in length) in the mutant complex structure (Fig. 4B). In addition, the N-

14

262 terminus of the enzyme interacts with both E166 and the backbone carbonyl group of F140, and

263 plays an important role in maintaining the structural stability of the enzyme active site. The

264 E166R mutation eliminates the salt bridge with the N-terminus of the adjacent protomer, and

265 further introduces electrostatic repulsion leading to small yet significant changes in the N-

266 terminus conformation. Consequently, the distance between the N-terminal amine group and the

267 F140 carbonyl group increased from 2.6 Å in the WT to 3.7 Å in the M^{pro} E166R mutant,

268 diminishing the HB. This in turn may destabilize the loop that F140 resides on and also contains

269 other important structural features involved in enzyme catalysis and ligand binding, including the

270 backbone amide groups of Gly143 and Ser144 that form part of the oxyanion hole to stabilize the

271 reaction transition state. This loop also contains the peptide bond between Leu141 and Asn142

272 that interacts with the two extra carbon atoms of the inhibitor pyrrolidone ring, but not with the

273 substrate glutamine side chain. Destabilization of the region near F140 may increase the entropic

274 cost of binding to the rigid pyrrolidone ring of nirmatrelvir and GC-376, more than the smaller

275 and more flexible substrate glutamine side chain. For similar entropic reasons, the HB between

276 the pyrrolidone ring and E166 might contribute more to inhibitor binding than that between the

277 more flexible glutamine side chain and E166 (Fig. 4B). Consequently, the E166R mutation may

278 have a stronger effect on binding to inhibitors such as nirmatrelvir versus substrate.

279

280 **Discussion**

281 In sum, we demonstrate that using yeast growth as a proxy for M^{pro} activity can be a

282 reliable indicator of the effects that mutations in M^{pro} can have on its activity and potential for

283 drug resistance. Yeast assays indicated that an E166R mutation was resistant to nirmatrelvir and

284 *in vitro* enzyme assays confirmed this observation, revealing a ~1600-fold increase in resistance.

285 Furthermore, the C145A catalytic mutant[2] and E166N mutant did not cause a growth reduction

286 in yeast and enzyme assays showed that the E166N substitution confers a dramatic ~83-fold

287 decrease in activity. In yeast assays the N142A mutant displayed minor differences in drug

288 sensitivity compared to wild-type (RC_{50} ~1.5-fold more than WT), which was confirmed by our

289 *in vitro* enzyme assays. Similarly, the P132H mutant remained sensitive to nirmatrelvir based on

290 our yeast assay, potentially even more sensitive with an RC_{50} ~2.8-fold less than WT. This is

291 consistent with previous reports showing that the P132H mutant remains sensitive to nirmatrelvir

292 in *in vitro* enzyme assays [25-28]. It appears that M^{pro} mutants (i.e. E166R) that have a decrease in

293 catalytic efficiencies of up to 16-fold compared to WT are still able to confer a marked reduction

294 in yeast growth. This is important as resistant mutants are likely to reduce protein fitness [29,30].

295 However, the yeast assay is unable to detect enhanced M^{pro} activity (e.g., M^{pro} N142A), which

296 we observed in *in vitro* assays. This may have been due to the relatively small increase (1.4-

297 fold). However, the enhanced activity associated with N142A suggests that M^{pro} can evolve to be

298 a more active enzyme. It is possible that mutants which enhance M^{pro} activity can improve

299 protein fitness when combined with resistant mutants that on their own may have reduced

300 activity[14]. The crystal structure of E166R with GC-376 revealed loss of key hydrogen bonds with

301 the pyrrolidone ring of GC-376 which can explain the increase in resistance to nirmatrelvir

302 containing the same functional group. On the other hand, the E166N mutant which could be

303 considered a more conserved change than E166R decreased activity by ~83-fold and did not

304 confer a growth reduction in the yeast assays. In turn the crystal structure shows that the

305 asparagine prevents substrate binding through a new hydrogen bond with H163, providing a

306 mechanism to explain the significant reduction in activity. The additional mutants at E166 that

307 are associated with *in vitro* viral evolution experiments along with what we show here highlight

308 the importance of this site in playing a role in nirmatrelvir resistance. Our crystal structure

309 illuminates a structural mechanism to help explain how substitutions at E166 can either lead to

310 loss of activity versus gain of resistance.

311 While the drug doses used with yeast are in the micromolar versus nanomolar range that

312 is more typical of *in vitro* enzymatic or viral assays, we observed good correlations between the

313 yeast and enzymatic assays for nearly all of the mutants tested. The higher concentrations of drug

314 may be needed even though we deleted the major efflux pump, Pdr5, as yeast harbor a range of

315 efflux activities [31], or possibly differences in permeability as a result of lipid composition

316 differences from human cells, as well as potential drug interactions with the yeast cell wall [32].

317 Additional differences observed between the yeast and enzymatic assays may be a result of

318 having multiple substrates in yeast, additional complexity of the cellular proteome, differences in

319 pH, salt, and oxidation levels.

320 Taken together, these results demonstrate that a non-pathogenic, rapid, inexpensive and

321 highly accessible yeast-based method can be used to characterize mutants for both their effects

322 on M^{pro} activity and their responses to inhibitor compounds. There are reports using yeast as a

323 tool to screen for M^{pro} inhibitors or perform mutational analysis [33,34]. These systems incorporate

324 M^{pro} reporters and modification of M^{pro} to carry a N-terminal serine. Our work shows that

325 measuring the effects of M^{pro} (with a N-terminal methionine) on yeast growth (without any

326 reporters) can be a rapid and inexpensive approach to determine consequences of M^{pro} mutations

327 on activity and drug response. The qualitative results from the yeast assays can be an important

328 tool to help prioritize mutants of interest before moving ahead to more demanding viral based

329 experiments. As more inhibitors are used in the general population there will be increasing

330 selection pressures for drug resistant mutations that will go beyond the current set of mutants that

331   are potentially drug resistant[35,36]. The yeast system reported here promises to be an invaluable

332   tool in helping to combat future drug resistant mutations to stem the tide of COVID-19

333   infections.

334

335   **Materials and Methods**

336   **Strains, media, and chemicals**

337   All yeast strains carried a *pdr5*::*G418* deletion in the BY4741 background (*MATa his3Δ1 leu2Δ0*

338   *met15Δ0 ura3Δ0*). Yeast were grown in liquid synthetic complete (SC) media (0.17% yeast

339   nitrogen base, 0.5% ammonium sulfate, amino acid mix with appropriate drop out as noted, 2%

340   glucose) or on solid SC media containing 2% agar at 30°C. Media and reagents for culturing

341   yeast were from United States Biological (Salem, MA). M^{pro} and PL^{pro} inhibitors were from

342   MedChemExpress (Monmouth Junction, NJ) and Selleck Chemicals (Houston, TX). All other

343   chemicals were from Sigma Aldrich (St. Louis, MO) or VWR (Radnor, PA).

344

345   **Expression of SARS-CoV-2 genes in yeast and mutagenesis**

346   The indicated SARS-CoV-2 genes were codon optimized for yeast, tagged at the 3' with a 3X-

347   Flag epitope, carried on high copy plasmids and genes were under the control of the Gal1

348   promoter (see Table S2). Site directed mutagenesis was performed using In-Fusion Cloning Kit

349   (Takara). Primers used for mutagenesis can be found in Table S3. The M^{pro} gene was sequenced

350   to confirm that mutations were incorporated successfully.

351

18

Yeast Transformation

A single yeast colony was used to inoculate 5ml liquid YPD (1% yeast extract, 1% yeast bacto-peptone, 2% glucose) and grown overnight at 30°C. The next day cells were washed and resuspended in 1ml lithium acetate/TE solution (100 mM lithium acetate, 10 mM Tris-HCl, 1 mM EDTA, pH 7.5). Cells were aliquoted (60 µl) into microcentrifuge tubes, followed by the addition of denatured salmon sperm DNA (50µg), 0.2µg of plasmid, 1ml polyethylene glycol (PEG) lithium acetate solution (40% (w/v) PEG 4000, 100 mM lithium acetate, 10 mM Tris-HCl, 1 mM EDTA, pH 7.5), and incubated for 45min at 30°C. This was followed by a 20min incubation at 42° and chilled for 2min on ice. Cells were washed and resuspended in 100µl H_2O and plated on selective SC agar plates, incubated for ~3 days at 30°C.

Protein extraction and western analysis

Cells were grown overnight in 5 ml SC-Ura, 2% raffinose at 30°C. The next day, fresh cultures were started with optical density OD_{600} of 0.5 in 20 ml SC-Ura, 2% galactose at 30° for 6 hrs. Cells were then harvested, frozen in liquid nitrogen, and stored at −80°. For total protein extract, trichloroacetic acid was performed as described previously [37] and protein concentration was determined by BCA protein assay kit (Thermo scientific). Protein samples were separated by 4–12% gradient SDS-PAGE (GenScript) and blotted onto nitrocellulose or PVDF membranes. The following primary antibodies were used at 1:5000 dilution: anti-FLAG antibody (GenScript), and anti-GAPDH antibody (Proteintech). Secondary anti-mouse IgG HRP antibody was used at 1:7000 dilution (Promega). ChemiDoc (Bio-Rad) imaging system was used to detect chemiluminescence signals from blots.

19

Cell growth assays and RC$_{50}$ measurements

Cells were grown overnight in 5ml SC-Ura, 2% raffinose at 30°C. The next day, fresh cultures were started with an OD$_{600}$ of 0.1 in SC-Ura, 2% galactose, with or without inhibitors and transferred to to 96-well plates, incubated at 30°C on a a rotary shaker. Three independent transformants were used to test each form of M^{pro}. Each transformant was sampled three times for each assay. The plate was transferred to a Tecan Infinite 200 PRO plate reader, and OD$_{600}$ measurements were taken at 0, 24, 48 and 72 hours, with 5 flashes per well. Excel (Microsoft) was used to analyze the raw data. As a measure of inhibitory activity of nirmatrelvir we calculated a Recovery Concentration (RC$_{50}$). The slopes from the dose responses were calculated and used to estimate the concentration of inhibitor that improves growth to half-maximal relative to empty vector control after 72 hours of growth.

Yeast Proteomics

Cells were grown overnight in 10ml SC-Ura + 2% Raffinose media at 30°C. The next day, fresh cultures were started with OD$_{600}$ of 0.1 in 100ml SC-Ura + 2% galactose at 30°C for 6 hr. Cells were then harvested, frozen in liquid nitrogen, and stored at −80°. Protein extraction was performed as described previously[37] and protein concentration was determined using Pierce BCA protein assay kit (Thermo scientific).

To determine changes in the proteome associated with expression of M^{pro} versus M^{pro} C145A, in-solution tryptic digestion was performed as described[38] followed by desalting with a Pierce Peptide Desalting Spin Columns per the manufacturer's protocol (ThermoFisher Scientific, cat no. 89852) and the peptides were dried by vacuum centrifugation. 600 ng of the final sample was analyzed by mass spectrometry. HPLC-ESI-MS/MS was performed as previously described[39].

398   In brief, MS/MS was performed in positive ion mode on a Thermo Scientific Orbitrap Fusion

399   Lumos tribrid mass spectrometer fitted with an EASY-Spray Source (Thermo Scientific, San Jose,

400   CA). NanoLC was performed using a Thermo Scientific UltiMate 3000 RSLCnano System with

401   an EASY Spray C18 LC column (Thermo Scientific).

402   Tandem mass spectra were extracted from Xcalibur 'RAW' files and charge states were

403   assigned using the ProteoWizard 2.1.x msConvert script using the default parameters(23). The

404   fragment mass spectra were then searched against the *Saccharomyces cerevisiae* (strain ATCC

405   204508 / S288c) (Baker's yeast) UniProt database (6067 entries) using Mascot (Matrix Science,

406   London, UK; version 2.6) using the default probability cut-off score. Cross-correlation of Mascot

407   search results with X! Tandem was accomplished with Scaffold (version Scaffold_4.8.7;

408   Proteome Software, Portland, OR, USA). Probability assessment of peptide assignments and

409   protein identifications were made through the use of Scaffold. Only peptides with ≥ 95%

410   probability were considered. Progenesis QI for proteomics software (version 2.4, Nonlinear

411   Dynamics Ltd., Newcastle upon Tyne, UK) was used to perform ion-intensity based label-free

412   quantification similar to as previously described[39]. Principal component analysis and unbiased

413   hierarchal clustering analysis (heat map) was performed in Perseus[40,41]. Gene ontology and

414   KEGG pathway enrichment analysis was performed with DAVID[42].

415

416   **Recombinant Mpro and proteolytic activity assays**

417   SARS-CoV-2 M[pro] mutants were generated with QuikChange® II Site-Directed Mutagenesis Kit

418   from Agilent (Catalog #200524), using plasmid pE-SUMO-Mpro as the template. The plasmid

419   produces tag-free Mpro protein with no extra residue at either N- or C-terminus upon removal of

420   the SUMO tag by SUMO protease digestion[17].

421   SARS-CoV-2 M^{pro} mutant proteins were expressed and purified as previously

422   described[17,24] with minor modifications. Plasmids were transformed into E. coli BL21(DE3)

423   competent cells and bacterial cultures overexpressing the target proteins were grown in LB

424   (Luria-Bertani) medium containing 50 µg/mL of kanamycin at 37 °C, and expression of the

425   target protein was induced at an optical density (A600) of 0.6-0.8 by the addition of isopropyl β-

426   d-1-thiogalactopyranoside (IPTG) to a final concentration of 0.5 mM. The cell culture was

427   incubated at 18°C for 12-16 hrs. Bacterial cultures were harvested by centrifugation (8,000 ×g,

428   10 min, 4°C) and resuspended in lysis buffer containing 25 mM Tris (pH 8.0), 750 mM NaCl,

429   2 mM DTT, 0.5 mg/mL lysozyme, 0.5 mM phenylmethylsulfonyl fluoride (PMSF) and

430   0.02 mg/mL DNase I. Bacterial cells were lysed by alternating sonication (30% amplitude, 1 s

431   on/1 s off) and homogenization using a tissue grinder. The lysed cell suspension was clarified by

432   centrifugation (18,000 ×g, 30min, 4°C) and the supernatant was incubated with Ni-NTA resin for

433   over 2 hrs at 4°C on a rotator. The Ni-NTA resin was thoroughly washed with 20 mM imidazole

434   in washing buffer containing 50mM Tris (pH 8.0), 150mM NaCl, 2 mM DTT, and SUMO-M^{pro}

435   protein was eluted with elution buffer containing 50 to 300mM imidazole, 50mM Tris (pH 8.0),

436   150mM NaCl, 2mM DTT. Fractions containing SUMO-M^{pro} proteins greater than 90%

437   homogeneity were pooled and subjected to dialysis (two times) against a buffer containing

438   50mM Tris (pH 8.0), 150mM NaCl, 2mM DTT and 10% glycerol. SUMO protease digestion

439   was carried out at 30ºC for 1 hr to remove SUMO tag. Following digestion, SUMO Protease and

440   SUMO tag were removed by Ni-NTA resin. The purified tag-free SARS-CoV-2 Mpro mutant

441   proteins were fast frozen in liquid nitrogen and stored at -80 °C.

442   For measurement of K_m/V_{max} of SARS-CoV-2 M^{pro} mutants, proteolytic reactions were

443   carried out with optimized concentrations of the mutant proteins and a series of concentrations of

444   FRET substrate ranging from 0 to 200 µM in 100µL of reaction buffer containing 20mM HEPES

445   (pH 6.5), 120mM NaCl, 0.4mM EDTA, 4mM DTT, and 20% glycerol at 30°C in a BioTek

446   Cytation 5 imaging reader (Agilent) with filters for excitation at 360/40 nm and emission at

447   460/40 nm. Reactions were monitored every 90s, and the initial velocity of the proteolytic

448   activity was calculated by linear regression for the first 15min of the kinetic progress curves. The

449   initial velocity was plotted against the FRET substrate concentrations using the classic

450   Michaelis-Menten equation in Prism 8 software.

451   For IC_{50} measurements, optimized concentrations of the mutant proteins were incubated

452   with series concentrations of GC-376, PF-00835231 or nirmatrelvir (PF-07321332) in 100µL of

453   reaction buffer at 30°C for 15 min, and the reaction was initiated by adding 10µM FRET

454   substrate. The reaction was monitored for 1 hr, and the initial velocity was calculated for the first

455   15min by linear regression. The IC_{50} was determined by plotting the initial velocity against

456   various concentrations of the compounds using log (inhibitor) vs response-variable slope in

457   Prism 8 software.

458   For K_i measurements, optimized concentrations of the mutant proteins were added to

459   20µM FRET substrate with various concentrations of GC-376, PF-00835231 or nirmatrelvir (PF-

460   07321332) in 200µL of reaction buffer at 30°C to initiate the proteolytic reaction. The reaction

461   was monitored for 2 hrs and the initial velocity was calculated for the first 90 min by linear

462   regression. The K_i was calculated by plotting the initial velocity against various concentrations of

463   the compounds using Morrison plot (tight binding) in Prism 8 software.

464

Mpro crystallization and structure determination

SARS-CoV-2 Mpro E166N/R was diluted to 5 mg/mL in protein buffer (50 mM Tris pH 7.0, 150

mM NaCl, 4 mM DTT). Protein for complex determination was incubated overnight at 4 °C with

2mM GC376. No precipitation was observed after incubation, and centrifugation was not

necessary. Apo and complex crystals were grown using 1.5 μL:1.5 μL (protein:well solution)

hanging drops and a well solution of 0.1 M MgCl$_2$, 20% PEG 3350, 10% 1,6-hexanediol, 0.1 M

HEPES pH 7.5, and 0.1 M LiSO$_4$. E166N/R crystals grew overnight at 20 °C. Crystals were

cryoprotected using the well solution supplemented with 20% glycerol, and then flash-frozen in

liquid nitrogen.

X-ray diffraction data (Table S4) were collected at the Southeast Regional Collaborative

Access Team (SER-CAT) 22-BM beamline at the Advanced Photon Source (APS) in Argonne,

IL, and processed with HKL2000 and CCP4. PHASER was used for molecular replacement

using a previously solved SARS-CoV-2 Mpro structure (PDB ID: 7LYH) as a reference model.

The CCP4 suite, (23) Coot, (24) and the PDB REDO server (pdb-redo.eu) (25) were used to

complete the model building and refinement. The PyMOL Molecular Graphics System

(Schrödinger, LLC) was used to generate all images.

494

495   **Author Contributions**

496   J.S.C, Y.C., J.W. conceived the project, analyzed, and interpreted data. J.O. performed all yeast

497   experiments. X.Z. constructed and purified mutants. R.T.M. crystallized mutants. E.M.L.

498   analyzed crystals, collected diffraction data and determined the structures with assistance from

499   L.M.C.J., M.J.B. YH and HT performed protein expression, purification and enzyme assays.

500   A.A.L. and P.L. performed mass spectrometry and analysis. J.S.C. wrote the manuscript with

501   input from Y.C. and J.W.

502

503   **Competing Interests**

504   The authors declare no competing interests.

505

506   **Data Accessibility**

507   The X-ray crystal structures have been deposited into the Protein Data Bank with accession

508   codes 8DDI (E166N Apo) and 8DDM (E166R GC376).

509

510

25

References

1. Ng, T. I. *et al.* Antiviral Drug Discovery for the Treatment of COVID-19 Infections. *Viruses*
    14, doi:10.3390/v14050961 (2022).

2. Jin, Z. *et al.* Structure of M(pro) from SARS-CoV-2 and discovery of its inhibitors. *Nature*
    582, 289-293, doi:10.1038/s41586-020-2223-y (2020).

3. Chia, C. S. B., Xu, W. & Shuyi Ng, P. A Patent Review on SARS Coronavirus Main
    Protease (3CL(pro)) Inhibitors. *ChemMedChem* **17**, e202100576,
    doi:10.1002/cmdc.202100576 (2022).

4. Hung, H. C. *et al.* Discovery of M Protease Inhibitors Encoded by SARS-CoV-2. *Antimicrob*
    Agents Chemother **64**, doi:10.1128/AAC.00872-20 (2020).

5. Morse, J. W., Gladkikh, T. M., Hackenburg, D. M. & Gould, R. K. COVID-19 and human-
    nature relationships: Vermonters' activities in nature and associated nonmaterial values
    during the pandemic. *PLoS One* **15**, e0243697, doi:10.1371/journal.pone.0243697 (2020).

6. FDA. *Fact sheet for healthcare providers: Emergency use authorization for Paxlovid*
    , <https://www.fda.gov/media/155050/download.> (2021).

7. Owen, D. R. *et al.* An oral SARS-CoV-2 M(pro) inhibitor clinical candidate for the treatment
    of COVID-19. *Science* **374**, 1586-1593, doi:10.1126/science.abl4784 (2021).

8. Hammond, J. *et al.* Oral Nirmatrelvir for High-Risk, Nonhospitalized Adults with Covid-19.
    N Engl J Med **386**, 1397-1408, doi:10.1056/NEJMoa2118542 (2022).

9. Boras, B. *et al.* Preclinical characterization of an intravenous coronavirus 3CL protease
    inhibitor for the potential treatment of COVID19. *Nat Commun* **12**, 6055,
    doi:10.1038/s41467-021-26239-2 (2021).

533   10. Cully, M. A tale of two antiviral targets - and the COVID-19 drugs that bind them. *Nat Rev*

534   *Drug Discov* **21**, 3-5, doi:10.1038/d41573-021-00202-8 (2022).

535   11. CDC. *Information for laboratories about Coronavirus (COVID-19).*

536   <https://www.cdc.gov/coronavirus/2019-ncov/lab/lab-biosafety-guidelines.html> (2020).

537   12. Zhu, W. *et al.* Identification of SARS-CoV-2 3CL Protease Inhibitors by a Quantitative

538   High-Throughput Screening. *ACS Pharmacol Transl Sci* **3**, 1008-1016,

539   doi:10.1021/acsptsci.0c00108 (2020).

540   13. Jochmans, D. *et al.* The substitutions L50F, E166A and L167F in SARS-CoV-2 3CLpro are

541   selected by a protease inhibitor in vitro and confer resistance to nirmatrelvir.

542   *bioRxiv*, 2022.2006.2007.495116, doi:10.1101/2022.06.07.495116 (2022).

543   14. Zhou, Y. *et al.* Nirmatrelvir Resistant SARS-CoV-2 Variants with High Fitness in Vitro.

544   *bioRxiv*, 2022.2006.2006.494921, doi:10.1101/2022.06.06.494921 (2022).

545   15. V'Kovski, P., Kratzel, A., Steiner, S., Stalder, H. & Thiel, V. Coronavirus biology and

546   replication: implications for SARS-CoV-2. *Nat Rev Microbiol* **19**, 155-170,

547   doi:10.1038/s41579-020-00468-6 (2021).

548   16. Kneller, D. W. *et al.* Structural plasticity of SARS-CoV-2 3CL M(pro) active site cavity

549   revealed by room temperature X-ray crystallography. *Nat Commun* **11**, 3202,

550   doi:10.1038/s41467-020-16954-7 (2020).

551   17. Sacco, M. D. *et al.* Structure and inhibition of the SARS-CoV-2 main protease reveal

552   strategy for developing dual inhibitors against M(pro) and cathepsin L. *Sci Adv* **6**,

553   doi:10.1126/sciadv.abe0751 (2020).

554   18. Fu, Z. *et al.* The complex structure of GRL0617 and SARS-CoV-2 PLpro reveals a hot spot

555   for antiviral drug discovery. *Nat Commun* **12**, 488, doi:10.1038/s41467-020-20718-8 (2021).

556   19. Shaqra, A. M. *et al.* Defining the substrate envelope of SARS-CoV-2 main protease to

557   predict and avoid drug resistance. *Nat Commun* **13**, 3556, doi:10.1038/s41467-022-31210-w

558   (2022).

559   20. Matthew, A. N. *et al.* Drug Design Strategies to Avoid Resistance in Direct-Acting Antivirals

560   and Beyond. *Chem Rev* **121**, 3238-3270, doi:10.1021/acs.chemrev.0c00648 (2021).

561   21. Xiong, M. *et al.* What coronavirus 3C-like protease tells us: From structure, substrate

562   selectivity, to inhibitor design. *Med Res Rev* **41**, 1965-1998, doi:10.1002/med.21783 (2021).

563   22. MacDonald, E. A. *et al.* Recognition of Divergent Viral Substrates by the SARS-CoV-2

564   Main Protease. *ACS Infect Dis* **7**, 2591-2595, doi:10.1021/acsinfecdis.1c00237 (2021).

565   23. Xue, X. *et al.* Structures of two coronavirus main proteases: implications for substrate

566   binding and antiviral drug design. *J Virol* **82**, 2515-2527, doi:10.1128/JVI.02114-07 (2008).

567   24. Hu, Y. *et al.* Boceprevir, calpain inhibitors II and XII, and GC-376 have broad-spectrum

568   antiviral activity against coronaviruses in cell culture. *bioRxiv*,

569   doi:10.1101/2020.10.30.362335 (2020).

570   25. Greasley, S. E. *et al.* Structural basis for the in vitro efficacy of nirmatrelvir against SARS-

571   CoV-2 variants. *J Biol Chem* **298**, 101972, doi:10.1016/j.jbc.2022.101972 (2022).

572   26. Sacco, M. D. *et al.* The P132H mutation in the main protease of Omicron SARS-CoV-2

573   decreases thermal stability without compromising catalysis or small-molecule drug

574   inhibition. *Cell Res* **32**, 498-500, doi:10.1038/s41422-022-00640-y (2022).

575   27. Ullrich, S., Ekanayake, K. B., Otting, G. & Nitsche, C. Main protease mutants of SARS-

576   CoV-2 variants remain susceptible to nirmatrelvir. *Bioorg Med Chem Lett* **62**, 128629,

577   doi:10.1016/j.bmcl.2022.128629 (2022).

578   28. Li, P. *et al.* SARS-CoV-2 Omicron variant is highly sensitive to molnupiravir, nirmatrelvir,

579   and the combination. *Cell Res* **32**, 322-324, doi:10.1038/s41422-022-00618-w (2022).

580   29. Chang, M. W. & Torbett, B. E. Accessory mutations maintain stability in drug-resistant HIV-

581   1 protease. *J Mol Biol* **410**, 756-760, doi:10.1016/j.jmb.2011.03.038 (2011).

582   30. De Luca, A. in *Antiretroviral Resistance in Clinical Practice* (ed A. M. Geretti) (2006).

583   31. Sa-Correia, I. & Godinho, C. P. Exploring the biological function of efflux pumps for the

584   development of superior industrial yeasts. *Curr Opin Biotechnol* **74**, 32-41,

585   doi:10.1016/j.copbio.2021.10.014 (2022).

586   32. Mukhopadhyay, K., Kohli, A. & Prasad, R. Drug susceptibilities of yeast cells are affected

587   by membrane lipid composition. *Antimicrob Agents Chemother* **46**, 3695-3705,

588   doi:10.1128/AAC.46.12.3695-3705.2002 (2002).

589   33. Alalam, H. *et al.* A Genetic Trap in Yeast for Inhibitors of SARS-CoV-2 Main Protease.

590   *mSystems* **6**, e0108721, doi:10.1128/mSystems.01087-21 (2021).

591   34. Flynn, J. M. *et al.* Comprehensive fitness landscape of SARS-CoV-2 M(pro) reveals insights

592   into viral resistance mechanisms. *Elife* **11**, doi:10.7554/eLife.77433 (2022).

593   35. Padhi, A. K. & Tripathi, T. Hotspot residues and resistance mutations in the nirmatrelvir-

594   binding site of SARS-CoV-2 main protease: Design, identification, and correlation with

595   globally circulating viral genomes. *bioRxiv*, 2022.2007.2012.499687,

596   doi:10.1101/2022.07.12.499687 (2022).

597   36. Hu, Y. *et al.* Naturally occurring mutations of SARS-CoV-2 main protease confer drug

598   resistance to nirmatrelvir. *bioRxiv*, 2022.2006.2028.497978, doi:10.1101/2022.06.28.497978

599   (2022).

600   37. Shah, S. B. *et al.* Glucose Signaling Is Connected to Chromosome Segregation Through

601   Protein Kinase A Phosphorylation of the Dam1 Kinetochore Subunit in Saccharomyces

602   cerevisiae. *Genetics* **211**, 531-547, doi:10.1534/genetics.118.301727 (2019).

603   38. Pendleton, A. L. *et al.* Lower oxygen consumption and Complex I activity in mitochondria

604   isolated from skeletal muscle of fetal sheep with intrauterine growth restriction. *Am J Physiol*

605   *Endocrinol Metab* **319**, E67-E80, doi:10.1152/ajpendo.00057.2020 (2020).

606   39. Parker, S. S. *et al.* Insulin Induces Microtubule Stabilization and Regulates the Microtubule

607   Plus-end Tracking Protein Network in Adipocytes. *Mol Cell Proteomics* **18**, 1363-1381,

608   doi:10.1074/mcp.RA119.001450 (2019).

609   40. Tyanova, S. *et al.* The Perseus computational platform for comprehensive analysis of

610   (prote)omics data. *Nat Methods* **13**, 731-740, doi:10.1038/nmeth.3901 (2016).

611   41. Tyanova, S. & Cox, J. Perseus: A Bioinformatics Platform for Integrative Analysis of

612   Proteomics Data in Cancer Research. *Methods Mol Biol* **1711**, 133-148, doi:10.1007/978-1-

613   4939-7493-1_7 (2018).

614   42. Huang da, W., Sherman, B. T. & Lempicki, R. A. Systematic and integrative analysis of

615   large gene lists using DAVID bioinformatics resources. *Nat Protoc* **4**, 44-57,

616   doi:10.1038/nprot.2008.211 (2009).

Supplementary Files

This is a list of supplementary files associated with this preprint. Click to download.

- TableS1.xlsx
- SupplementaryMaterials.pdf